# Modeling methods for treatment planning in overlapping electroporation treatments

Enric Perera-Bel, Borja Mercadal, Tomás García-Sánchez, Miguel A. González Ballester, and
Antoni Ivorra

*Abstract— Objective:* **Irreversible electroporation (IRE) is a non-thermal tissue ablation therapy which is induced by applying high voltage waveforms across electrode pairs. When multiple electrode pairs are sequentially used, the treatment volume (TV) is typically computed as the geometric union of the TVs of individual pairs. However, this method neglects that some regions are exposed to overlapping treatments. Recently, a model describing cell survival probability was introduced which effectively predicted TV with overlapping fields *in vivo*. However, treatment overlap has yet to be quantified. This study characterizes TV overlap in a controlled *in vitro* setup with the two existing methods which are compared to an adapted logistic model proposed here.** *Methods*: **CHO cells were immobilized in agarose gel. Initially, we characterized the electric field threshold and the cell survival probability for overlapping treatments. Subsequently, we created a 2D setup where we compared and validated the accuracy of the different methods in predicting the TV.** *Results*: **Overlap can reduce the electric field threshold required to induce cell death, particularly for treatments with low pulse number. However, it does not have a major impact on TV in the models assayed here, and all the studied methods predict TV with similar accuracy.** *Conclusion*: **Treatment overlap has a minor influence in the TV for typical protocols found in IRE therapies.** *Significance*: **This study provides evidence that the modeling method used in most pre-clinical and clinical studies seems adequate.**

*Index Terms*—**Electroporation, overlap, multiple pairs, electric field threshold, cell survival model**

## I. Introduction

ELECTROPORATION is a phenomenon that affects the cell membrane by transitorily or permanently increasing its permeability to ions and macromolecules when the cell is exposed to a high electric field. Typically, such exposure consists in a series of pulses with a duration ranging from microseconds to a few milliseconds [1], [2]. Two outcomes can be defined: reversible electroporation, when the membrane recovers after field exposure and the cell remains viable, and irreversible electroporation, which causes cell death due to homeostasis loss, even if the cell membrane is capable of resealing. For the same electric field waveform, irreversible electroporation (IRE) occurs for a higher field magnitude than the magnitude required for reversible electroporation.

Tissue electroporation is the basis of several therapies. It is for instance used in two therapeutic approaches for solid tumor eradication: in electrochemotherapy (ECT) an anti-cancer drug can penetrate into malignant cells thanks to the increased permeabilization obtained in reversible electroporation [3]–[5], and in non-thermal irreversible electroporation (NTIRE) the malignant tissues are ablated by the effect of the local field with minimal thermal damage [6], [7]. Another application of reversible electroporation is electrogene therapy (EGT) where the highly permeable state is used to transfect vectors non-virally [8], [9]. In recent years, irreversible electroporation is also being investigated as a promising procedure for cardiac ablation [10], [11].

In recent years, electroporation therapies have greatly benefited from treatment planning [12], [13]. It is generally accepted that, for a given pulsing protocol and tissue, electroporation is induced upon surpassing an electric field threshold [2], [14]–[18]. The electric field distribution is highly dependent on the number of electrodes, their relative position, and the applied voltages [19], [20]. Thus, planning electroporation procedures consists in finding an electrode configuration that generates an electric field that surpasses the electric field threshold in the target tissue [21]–[24]. It is common to use up to 6 electrodes to be able to reach the whole target tissue. In such scenarios, planning consists of simulating the electric field distribution for each electrode pair, and the overall treatment volume (TV) is estimated as the superposition (i.e., geometrical union) of treatments by each individual pair. That is, if the tissue receives sufficient electric field from at least one pair it is considered to be treated, otherwise it is assumed to be left unaffected [25], [26].

It is known that with longer pulses, more pulses, or shorter inter-pulse pause, electroporation occurs at lower electric fields [18], [27]–[29]. Typically, protocols apply 10 to 100 consecutive pulses between each electrode pair to reduce the required field magnitude that induces electroporation. For a

given protocol, the threshold is determined by comparing numerical simulations to experimental data. However, most of the findings are based on 2-electrode setups, in contrast to actual treatments that can use up to 6 electrodes to cover the whole target tissue [21]–[24]. It is disputable that data obtained for 2-electrode setups can be directly translated for different configurations. By using more than one electrode pair, some regions of the tissue are treated multiple times with overlapping exposures (i.e., the tissue is treated with twice the pulse number, or more). Campelo *et al.* [30] characterized irreversible electroporation thresholds for prostate cancer tissue and found lower values than in similar studies that used less pairs. Among other reasons, they hypothesized that the lower field thresholds obtained were due to treatment overlap.

In a study involving irreversible electroporation in canine brain patients, Garcia *et al.* [31] proposed to model treatment overlap by, first, computing a scalar field of cell survival probability for each pair and, then, obtaining the field of probability of cell survival for the overall treatment by combining the individual fields by multiplication. In particular, they used a statistical model known as Peleg-Fermi equation to compute the cell survival probability as a function of the number of pulses [32]. This multiplication approach is not possible when treatment characterization is based on an electric field threshold because in this situation the outcome is binary (i.e., cells are intact below the threshold and treated above it). Instead, the Peleg-Fermi model characterizes the transition from dead (i.e., treated) to living cells (i.e., untreated). This same methodology for modeling overlapping treatments has been used in a numerical study for treatment planning optimization [33].

Whereas the Peleg-Fermi model has been validated for various cell lines and tissues with single pair setups (i.e., 2 electrodes) [27], [32], [34], [35], there are no reports validating the overlapping model based on the multiplication of cell survival probabilities in a controlled environment, nor it has been proven that it is better than the simpler method based on the geometrical union of TVs.

The goal of this work is to quantify cell death due to treatment overlap in electroporation-based therapies, and to explore and evaluate methodologies for predicting TV for such scenarios. We performed an *in vitro* study on a layer of Chinese hamster ovary (CHO) cells covered with agarose gel. The study was divided into two phases. The characterization phase consisted of characterizing the electric field threshold and the cell death probability for pulsing protocols equivalent to those conventionally used for ECT and NTIRE with two overlapping treatments. In the validation phase we created a 2D treatment scenario where we compared and validated the accuracy of three different methods in predicting cell death for overlapping treatments.

## II. METHODS

### A. Cellular preparations

CHO cells were cultured in a T75 flask in Dulbecco's Modified Eagle Medium (DMEM) supplemented with 10% fetal bovine serum and 1% penicillin/streptomycin. Cells were grown in a humidified incubator at 37 ℃ and 5% $CO_2$.
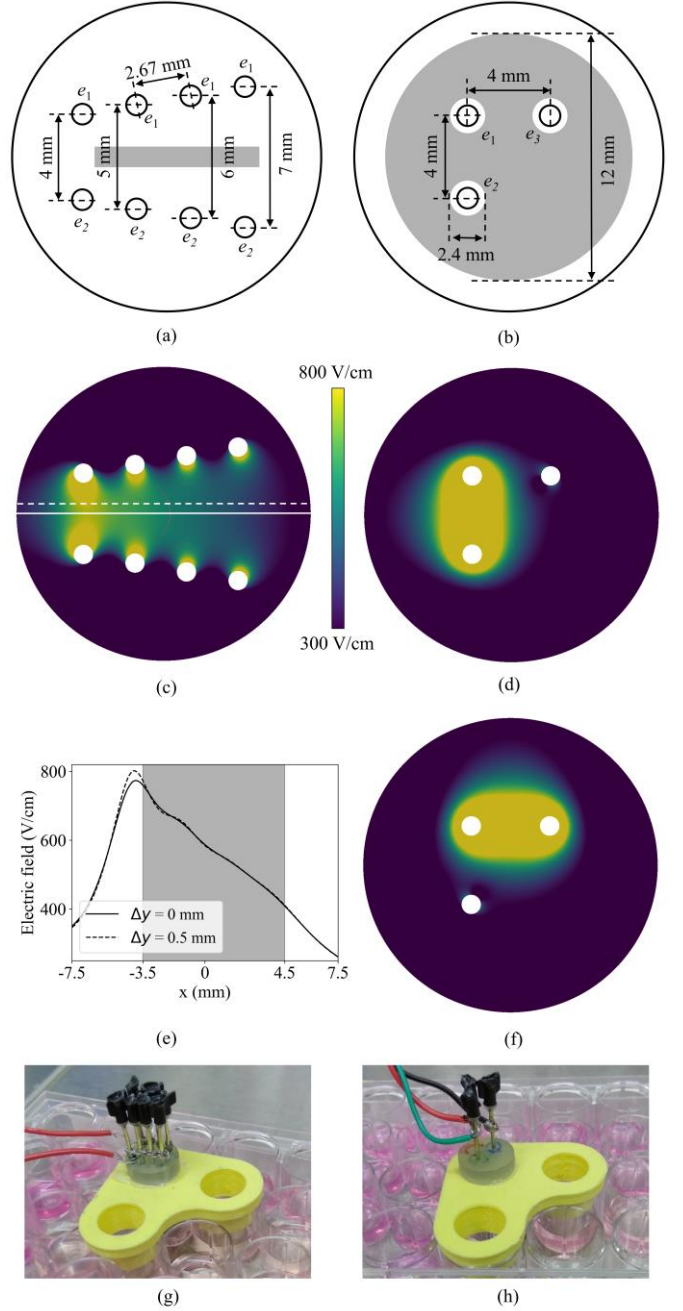


Fig. 1. Electrode configurations for the characterization (a, c, e, g) and the validation (b, d, f, h) phases. (a), (b): Sizing and disposition of the electrodes. The shaded region corresponds to the analyzed ROI. (c): Electric field simulation at 300 V and (e) its distribution alongside the x-axis (continuous line) and at 5-mm (dashed line). The analyzed ROI (8 mm × 1 mm, shaded) shows an almost linear electric field gradient. (d), (f): Electric field simulation at 500 V between $e_1$ and $e_2$, and between $e_3$ and $e_1$, respectively. (g), (h): photo of the electrodes and their 3D printed holders.

For preparing the samples for the assays, cells were initially washed with 2 ml of phosphate buffer saline (PBS). After a 2-minute trypsinization in 2 ml Trypsin at 37 ℃, 4 ml of complete DMEM were added and centrifuged at 1200 rpm for 5 minutes. Supernatant was removed and cells were resuspended in culture medium at concentration of $50 \times 10^3$ cells/ml. Cells were seeded in a 24-well plate at a concentration of $50 \times 10^3$ cells/well. After 24 hours, a thin layer of low gelling temperature agarose (1% in DMEM) was

TABLE I
PULSING PROTOCOLS

| Phase | Pulses per train | Voltages (100%) (V) | | |
|---|---|---|---|---|
| Characterization | 10 | 240 | 300 | 360 |
| | 100 | 160 | 220 | 280 |
| Validation | 10 | 400 | 500 | 600 |

deposited on top of each cell monolayer. Agarose was heated at 70 ºC-80 ºC to melt it and subsequently it was let to cool to 35 ºC. Then, culture medium from the plates containing the cells was replaced by 300 µl of agarose solution per well and the plate was stored in a fridge (7ºC) for 5 minutes to ensure full solidification of the gel. Consecutively, 100 µl of DMEM were added to the wells and the plate was reintroduced in the incubator for 1 hour. The purpose of the agarose layer was to immobilize living and dead cells to the bottom of the culture plates. Otherwise, cells dying during the upcoming electroporation treatments would float in the medium and displace.

Before the electrical treatments, the wells were rinsed twice (500 µl per rinse) with low conductivity buffer (250 mM sucrose, 10 mM glucose, 10 mM NaCl, 5 mM KCl, 2 mM MgCl$_2$, 10 mM HEPES, 1.8 mM CaCl$_2$, with pH 7.17, 2.5 mS/cm electrical conductivity, and osmolarity of 305 mOsm) to minimize electrolysis and thermal damage. The remaining buffer was removed, leaving only the adhered cells covered with the thin layer of agarose gel during pulsing. After the treatment, 360 µl of DMEM were added to the well and the plate was stored at the incubator for 3 hours.

All assays were repeated at least three times on different days to account for experimental variations.

*B. Pulsing protocols*

Fig. 1.a displays the electrode configuration for the characterization phase. Each electrode setup consisted of two short-circuited sets of 4 stainless steel needles with a diameter of 1 mm arranged in line (2.67 mm separation between consecutive needles). The two linear needles arrays were obliquely arranged; the closest needles were separated 4 mm and the two furthest 7 mm. A CNC machined polycarbonate structure was glued to a 3D printed template to aid in needle placement (Fig 1.g). This setup generated a linear electric field gradient along the horizontal axis in the central region between the two sets of electrodes. An 8 mm × 1 mm region of interest (ROI) along this x-axis was analyzed, hence, making it a 1D model (see Fig. 1.c and 1.e).

We defined two pulsing protocols equivalent to those typically used in ECT (trains of 10 pulses) and NTIRE (trains of 100 pulses). The pulses were applied at repetition frequency of 1 Hz and had a duration of 100 µs. Two trains of pulses (i.e., two treatments) were consecutively delivered. For each protocol, assays were performed with either a pause of 10 s or a pause of 1 minute between the two trains. These inter-train pauses were chosen according to what occurs during electroporation-based therapies with multiple pairs; between the activation of two consecutive pairs, it is required to wait for the generator to recharge (around 10 s), whereas non-consecutive pairs can be triggered one minute later (or more) after the first pair is completed.

In clinical electroporation procedures, it is typical to apply the same voltage-to-distance ratio across the different electrode pairs. Each portion of tissue then receives overlapping electric fields of different magnitudes (one magnitude per pair). Because the 1D model consisted of only one pair, we applied different voltages at each pulse train to generate two different electric fields. We applied a higher voltage in the first train and a lower voltage on the second (*H+L*), and vice versa (*L+H*). For each high voltage train, we applied a low voltage train at a ratio of 0, 0.25, 0.5, 0.75, and 1. For example, for a high voltage of 300 V, the voltage for a 0.25 ratio (25%) corresponds to $300 \times 0.25 = 75$ V. Since the relationship between the applied voltage and electric field is linear for a setup with constant electrical conductivity, these proportions can be directly translated to electric field magnitude. We refer as $E_H$ and $E_L$ to the electric field magnitudes generated with the high and low voltage trains, respectively. Notice that 0% indicates that no low pulse train was applied, i.e., 100%+0% and 0%+100% are the same case. Three different high voltages were assayed for each protocol to account for experimental variability (Table I).

This previous 1D model served to characterize the effects of treatment overlap, but it did not represent nor quantified the implications on real treatments. Thus, we validated the characterized models in a more realistic geometry. The validation assays consisted of a 2D setup with three-needle electrodes in a right-angled triangle pattern. The electrode distance was 4 mm and the diameter 1 mm (Fig. 1.b). The same voltage was applied in both pulse trains (100%+100%), but electrode activation was changed, treating first across $e_1$ and $e_2$ (Fig. 1.d), and the then across $e_3$ and $e_1$ (Fig. 1.f). A 12 mm diameter circle delimited the ROI. In addition, within 0.8 mm radius from the center of the electrode, we observed clear signs of electrolysis (gas bubbles and in some cases a bit of gel disruption) in the protocols with the highest voltages. We discarded this region where non-IRE damage was evident, plus a 0.4 mm safety margin (0.8 + 0.4 = 1.2 mm radius, Fig. 1.b). We only report validation results for the 10 pulse protocols because we did not observe any significant increase in cell death between one and two consecutive 100 pulse treatments in the characterization phase.

Needles were replaced if visual inspection revealed signs of corrosion.

*C. Imaging and Segmentation*

Three hours after pulsing, the cells were co-stained for an hour at room temperature with calcein AM at 1 µM and with propidium iodide (PI) at 15 µM. The cells were imaged in a Zeiss Cell Observer fluorescence microscopy station (Carl Zeiss, Oberkochen, Germany). Two-channel images were obtained; calcein AM (green) for living cells and PI (red) for dead cells. Since the treated area was larger than the microscope field of view, the region was divided in tiles which were later stitched together (Figs. 2.a and 2.c).

The images were segmented using Fiji ImageJ [36]–[38]. The green channel was binarized automatically by local thresholding using Bernsen's method [38], [39], and the red channel by the robust automatic threshold selection algorithm [40]. The watershed filter was applied to the binary images to separate adjacent cells, and an opening operation removed
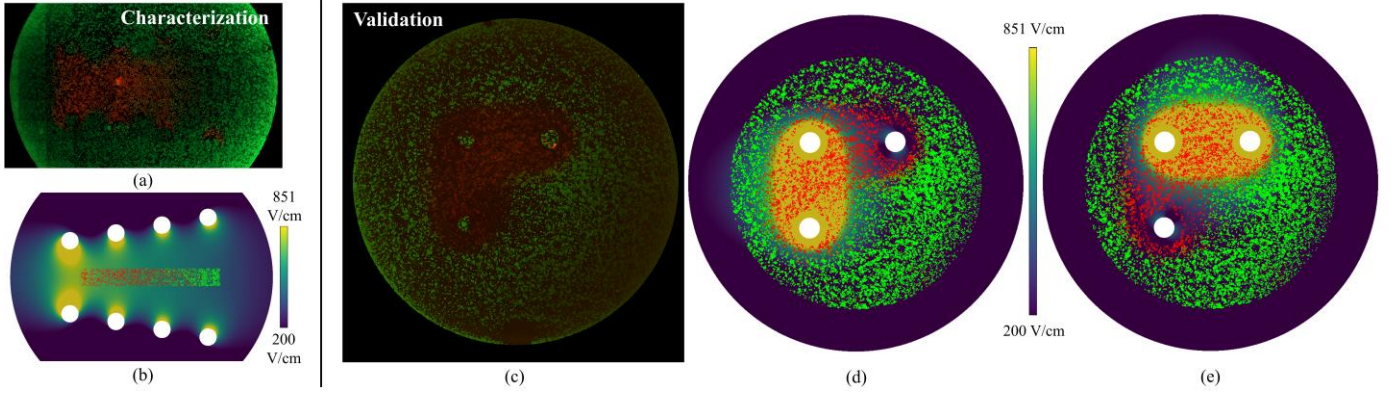
Fig. 2. Fluorescence images and segmentations of the characterization (a, b) and validation (c, d, e) setups. (a): fluorescence image of the characterization setup for two trains of 10 pulses at 300 V each with 10 s inter-pulse period with (b) the mapping of the segmented ROI to the electric field simulation. (c) fluorescence image of the validation setup with 10 pulse trains, 10 s protocol at 500 V with the segmented ROI overlayed on the electric field of the first pair (d) and of the second pair (e). The green channel corresponds to calcein AM staining (living cells) and the red channel to PI staining (dead cells). The 851 V/cm magnitude corresponds to the electric field threshold of a single 10 pulse train (found in this study).

remaining small particles. Lastly, the cells were filtered by size.

We numerically modeled the electric field. The segmented cell centroids were mapped to their corresponding locations in the simulated model to compare the state of the cell (alive/dead) with the received electric field (Figs. 2.b, 2.d, and 2.e). The electric field distribution was simulated with Elmer (https://www.csc.fi/web/elmer), an open-access multiphysics finite element solver, with the methodology described in [19] under the assumption of constant electrical conductivity.

### D. Characterization of cell survival

The standard electroporation model consists of simulating the electric field distribution to classify the electroporated tissue as the region with an electric field magnitude that surpasses a specific threshold. If multiple pairs are modelled, the electroporated tissue is simulated for each pair, and the overall TV is computed as the geometrical union of all the individual pairs.

Alternatively, cell death due to irreversible electroporation has been previously characterized using probabilistic models [27]. The probability of cell survival (or cell death) is modeled as a function of the electric field magnitude and describes the transition from living to dead cells. The Peleg-Fermi model has been widely used because it not only parametrizes the dependence with the field magnitude but also allows expressing cell survival as a function of the number of pulses [32]. However, since in the present work we independently evaluated protocols with a fixed number of pulses (either 10+10 or 100+100), the dependence on the number of pulses could be ignored. In such case, the Peleg-Fermi model becomes a logistic model (see supplementary materials). Hence, we used the logistic regression to fit the experimental data and characterize cell survival, which for a single pulse train ($S_t$) is defined as:

$$S_t = \frac{1}{1 + e^{-(\beta_0 + \beta_1 E)}} \tag{1}$$

where, coarsely, $\beta_0$ determines the field magnitude at which the transition from living to dead cells occurs and $\beta_1$ describes its slope. Cell death probability is then defined as $1 - S_t$.

Based on the above, we characterized cell survival in the cases in which two overlapping treatments were applied. We fitted (1) with the experimental data from the characterization (1D) setup for each of the $H+L$ and $L+H$ pulsing sequences independently. We used R (R Core Team) [41] with the generalized linear models (glm) [42] function to fit the data.

For every protocol, we derived the electric field threshold, which we determined to be the magnitude at which 95 % of cells were dead according to the fitted logistic regression. We also obtained a confidence interval of 3 times the standard error (3SE) of the logistic regression parameters ($\beta_0$ and $\beta_1$), which represented 99.7% of the deviation. We considered that two protocols were different if the 3SE intervals did not overlap.

Second, we modeled survival probability as a function of the two overlapping treatments. Garcia et al. [31] proposed to evaluate treatment overlap as the joint probability of individual treatments, i.e., the probability of survival was computed for each treatment independently and multiplied:

$$S_{overlap} = \prod_i S_{t,i} \tag{2}$$

In their work, they used the Peleg-Fermi model to obtain the survival probability for each treatment of spontaneous malignant glioma. However, the Peleg-Fermi model is only calibrated on a single treatment, which ignores any dependency between the overlapping electric fields. For this reason, we adapted the logistic regression (1) to also account for the overlapping treatment. A new parameter $\beta_2$ was added to characterize the influence of the second electric field in the survival probability. The adapted logistic model of overlapping treatments defines the survival probability ($S_{tt}$) as:

$$S_{tt,i} = \frac{1}{1 + e^{-(\beta_0 + \beta_1 E_i + \beta_2 E_j)}} \tag{3}$$

where $E_i$ is the electric field generated in treatment $i$ and $E_j$ is the electric field from the other treatment $j$. The contribution of all treatments is combined again with (2). For the present study with two treatments:

$$S_{overlap} = \prod_i S_{tt,i} = S_{tt,1} \cdot S_{tt,2}$$

TABLE II
ELECTRIC FIELD THRESHOLDS FOR TWO
TRAINS OF VARIABLE VOLTAGE AT 10 S AND 1 MIN INTER-PULSE PERIOD. THE
THRESHOLDS WERE DETERMINED TO BE THE MAGNITUDE AT WHICH 95 % OF
CELLS WERE DEAD ACCORDING TO THE LOGISTIC REGRESSIONS. SEE FIGURES
3 AND 4 FOR THE LOGISTIC CURVES.

| Pulses | Period | Voltage strength | Threshold (V/cm) | +3SE (V/cm) | -3SE (V/cm) |
|---|---|---|---|---|---|
| 10 + 10 | 10 s | 100%+0% | 851 | 876 | 828 |
| | | 100%+25% | 877 | 920 | 837 |
| | | 100%+50% | 807 | 846 | 771 |
| | | 100%+75% | 790 | 824 | 757 |
| | | 100%+100% | 711 | 741 | 682 |
| | | 100%+0% | 851 | 876 | 828 |
| | | 25%+100% | 844 | 882 | 807 |
| | | 50%+100% | 846 | 883 | 810 |
| | | 75%+100% | 796 | 831 | 763 |
| | | 100%+100% | 711 | 741 | 682 |
| | 1 min | 100%+0% | 851 | 876 | 828 |
| | | 100%+25% | 839 | 878 | 802 |
| | | 100%+50% | 807 | 846 | 770 |
| | | 100%+75% | 803 | 843 | 765 |
| | | 100%+100% | 773 | 802 | 745 |
| | | 100%+0% | 851 | 876 | 828 |
| | | 25%+100% | 805 | 838 | 773 |
| | | 50%+100% | 816 | 850 | 784 |
| | | 75%+100% | 831 | 867 | 798 |
| | | 100%+100% | 773 | 802 | 745 |
| 100 + 100 | - | 100%+0% | 613 | 634 | 593 |
| | 10 s | 100%+100% | 606 | 628 | 586 |
| | 1 min | 100%+100% | 621 | 643 | 599 |

$$S_{tt,1} = \frac{1}{1 + e^{-(\beta_0 + \beta_1 E_1 + \beta_2 E_2)}} \tag{4}$$
$$S_{tt,2} = \frac{1}{1 + e^{-(\beta_0 + \beta_1 E_2 + \beta_2 E_1)}}$$

We fitted this equation to characterize cell death as a function of the two overlapping electric fields. We used the data from all the $H+L$ and $L+H$ protocols, which contained all possible combinations of $E_H$ and $E_L$ fields. We only report fittings for the 10 pulse protocols since we did not observe any significant difference regarding cell survival between treatments consisting of one train or two trains of 100 pulses in the 1D configuration.

*E. Assessment of predictive accuracy*

We used the validation (2D) setup to analyze the predictive accuracy in overlapping treatments for three modeling methodologies: A) to model treatment overlap by obtaining the overall treatment volume (surface in this case) as the geometrical union of the individual treatments (as predicted by the field threshold criterion), B) to model treatment overlap by computing the field of cell survival probability as the product of the survival probability of individual treatments ($S_t$) (2), and C) to model treatment overlap by computing the field of cell survival probability as the product of the adapted logistic model of overlapping treatments $S_{tt}$ (4). Methods A and B are known, and method C is the new method we propose here. For method A we used the electric field thresholds obtained from the 100%+0% protocols. For method B we used the survival curve of the 100%+0% protocol. Method C was fitted with all the characterization data. The methods were only evaluated for the 10 pulse protocols.
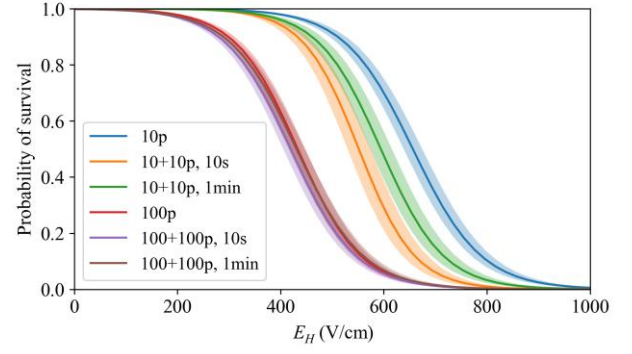


Fig. 3. Characterization of cell survival probability as a function of the electric field magnitude (1) when exposed to a single or two trains of 10 or 100 pulses. The assays were performed with three different voltages (Table I). In the cases of two trains, the voltage for both sequences was the same. The shading corresponds to ±3SE.

For each method, we computed the precision and miss rate metrics, as well as the Dice similarity coefficient:

$$Precision = \frac{TP}{TP + FP} \tag{5}$$
$$Miss\ rate = \frac{FN}{FN + TP} \tag{6}$$
$$Dice = \frac{2TP}{2TP + FP + FN} \tag{7}$$

TP is the true positive, TN the true negative, FP the false positive and FN the false negative. Additionally, we computed the area under the curve (AUC) of the receiver operating characteristic (ROC) curve to evaluate the overall classification accuracy regardless of the threshold [43]. Because we were predicting cell death, we considered dead cells as positives and living cells as negatives. For method A, a cell was classified as dead if it received an electric field above the IRE threshold. For methods B and C, a cell was classified as dead if its simulated probability of survival was below 5 %.

III. RESULTS

We first modeled cell survival as a function of the electric field (1) for a single pulse train (100 % + 0 %) and for two consecutive trains at $E_H$ (100 % + 100 %) (Table II and Fig. 3). On one hand, applying a second sequence of 10 pulses substantially reduced the electric field threshold from 851 V/cm to 773 V/cm with a 1 minute resting pause. The drop was even more accentuated with a 10 s pause, reaching 711 V/cm. This reduction was still observed considering the 3SE interval. On the other hand, no significant differences were observed in the 100 pulse protocols, with a single train threshold of 613 V/cm, and two train thresholds of 621 V/cm and 606 V/cm for 1 minute and 10 s inter-train pauses, respectively.

For the 10 pulse protocol, we characterized treatment overlap with two different electric fields by applying $H+L$ and $L+H$ trains. The results are presented in Table II and Fig. 4. In the 10 s group with $H+L$ pulsing, there is a tendency of higher cell death with $E_L$ of 50% and 75% (thresholds of 807 V/cm and 790 V/cm, respectively). However, the 3SE region of the 50% case overlaps with the 0% one. A similar trend is found
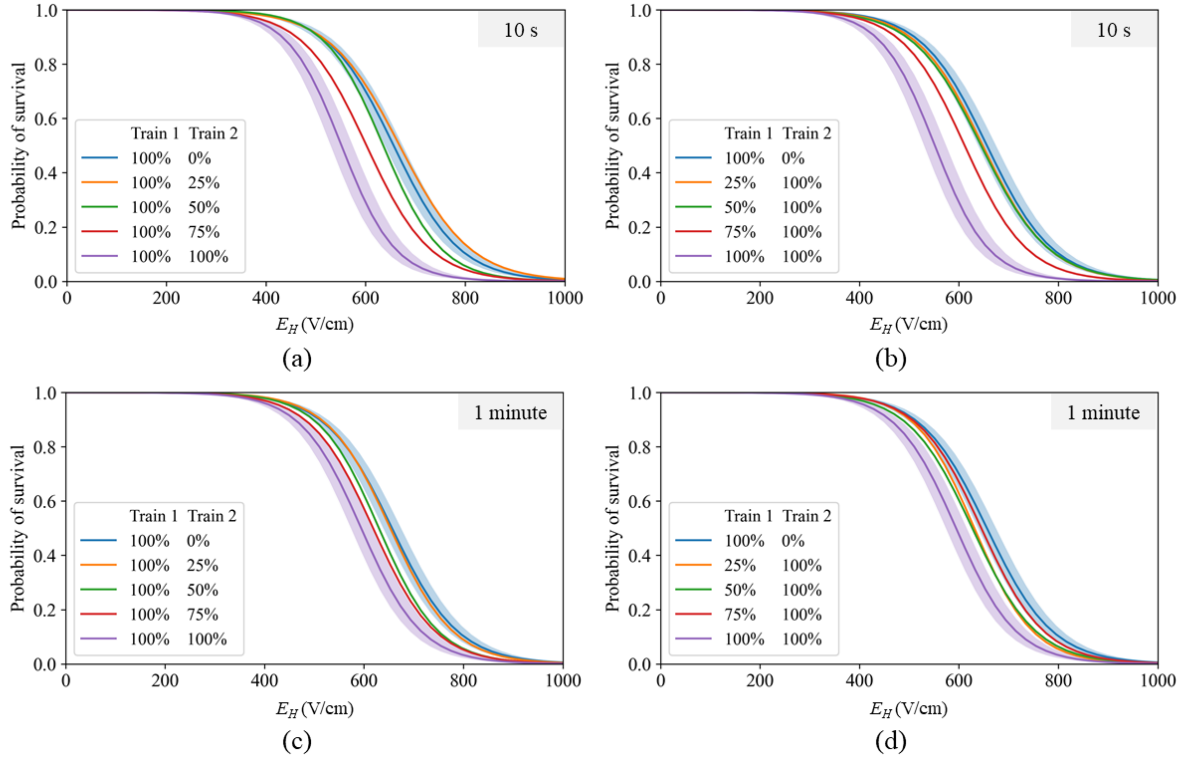
Fig. 4. Fitting of the survival probability of *H+L* (a, c) and *L+H* (b, d) trains (10 pulse trains). Inter-pulse period of 10s (a, b) and 1 min (c, d). The notation 0% is just to indicate that no voltage was applied. The shading corresponds to ±3SE interval of the fitting, and they are only represented in the 100%+0% and 100%+100% cases to ease image interpretation. All 3SE intervals are displayed in Table II.

with the 1 minute *H+L* protocols, but the intervals for all the combinations overlap with the 100%+0%. In the 10 s *L+H* case only $E_L$=75% presents a higher death ratio, and no effect is observed with a 1 min pause. These same findings can be observed in Fig. 4.a and 4.b where below $E_L$=50% the survival distribution does not change, but at 75% and 100% cells are killed at lower electric fields.

Fig. 5 displays a heatmap representation of survival probability for all the *H+L* and *L+H* protocols (colored stripes) and the predicted contours using the three proposed

methods. It can be observed that the method we propose here, C (dashed line), which truly models the effect of overlapping treatments ($S_{tt}$), fits the experimental data better than the method proposed by Garcia et al., B (solid line), in which the probability of survival for the overall treatment is computed as the product of the probability of survival of the individual treatments ($S_t$). (All the fitting parameters $\beta_0$, $\beta_1$, and $\beta_2$ can be found in Tables s.I and s.II in the supplementary materials.)

Fig. 6 shows heatmap representations of the survival density of the validation experiments. The results replicate the
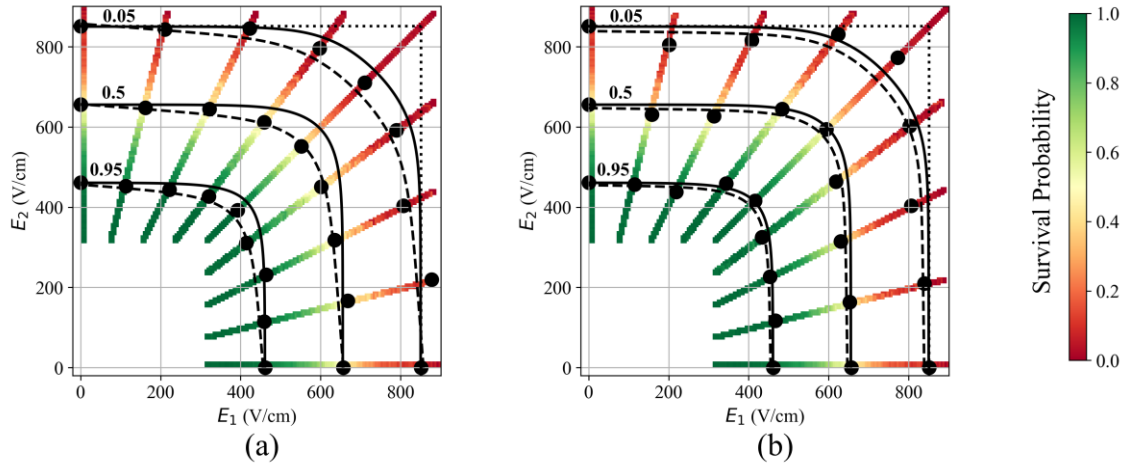


Fig. 5. Representations of experimental and modeled cell survival probabilities of the data from the characterization phase for the 10 pulse protocols at 10 s (a) and 1 minute (b) inter-pulse pauses. Each of the colormap stripes corresponds to experimental data from a *H+L* or *L+H* protocol, with the black circles being their probability of survival at 0.95, 0.5 and 0.05. The dotted line indicates the boundary for ensuring cell death (probability of survival = 0.05) according to the electric field threshold criterion (method A). The solid lines indicate isocontours of the probability of survival computed as the product of the survival probabilities of the two individual treatments (method B). Notice that method B is the same for 10 s and 1 minute pause treatments. The dashed lines indicate isocontours of the probability of survival computed as the product of the adapted logistic model of overlapping treatments (method C).
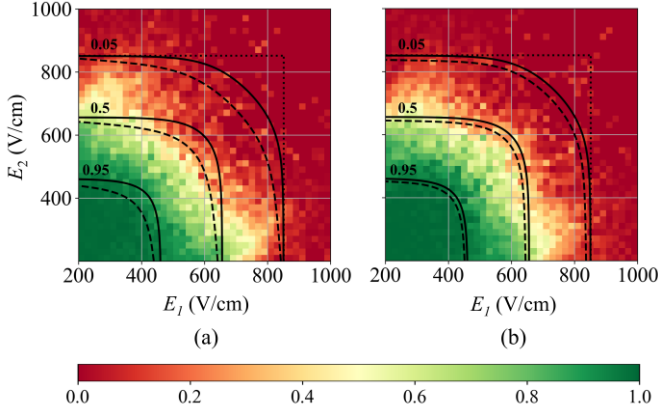
Fig. 6. Heatmap representations of cell survival density of the validation phase as a function of the field magnitudes of the two overlapping treatments. Treatment protocols of 10+10 pulses at 10 s (a) and at 1 min (b) inter-train pauses. $E_1$ corresponds to the electric field generated between $e_1$ and $e_2$ (Fig. 1.d) and $E_2$ is the field between $e_3$ and $e_1$ (Fig 1.f). The heatmap is divided in 20 V/cm bins. The dotted line displays the electric field threshold (method A). The 5 %, 50 %, and 95 % survival probabilities are represented in the solid and dashed lines for method B and C, respectively (same curves as in Fig. 5).

| Protocol | Method | Precision | Miss rate | Dice | AUC |
|---|---|---|---|---|---|
| 10+10 10 s | A | 0.986 | 0.343 | 0.788 | 0.961 |
| | B | 0.986 | 0.331 | 0.797 | 0.962 |
| | C | 0.982 | 0.300 | 0.818 | 0.964 |
| 10+10 1 min | A | 0.990 | 0.353 | 0.782 | 0.967 |
| | B | 0.989 | 0.341 | 0.791 | 0.968 |
| | C | 0.987 | 0.321 | 0.805 | 0.969 |

findings from the characterization models. Cells that received overlapping treatments with $E_L \geq 75\%$ showed a lower survival density, and a higher death ratio was accomplished with 10 s pause than with 1 minute pause.

The predictive accuracy of the three methods for modeling treatment overlap is indicated in Table III. All methods are equally good in classifying dead cells, with all of them having a precision > 0.982 and a maximum difference of 0.004. However, methods B and C classify slightly better the living cells over A, indicated by lower miss rate, which leads to an increased Dice score (0.009 percent points for B and 0.023-0.030 for C). Overall, all methods are very accurate at classifying the state of cells (alive or dead), with an AUC > 0.961 (and less than 0.003 difference between methods). These differences in classification are also displayed in Fig. 7 were we computed the predicted treatment area. In addition, in the supplementary materials, we included preliminary 3D simulations to evaluate the predicted IRE volume (Table s.IV and Figs. s.2 to s.4 in the supplementary materials).

In the 100 and 100+100 pulses protocols we observed signs of electrolysis around the needles, both in needles acting as anodes and in the needles acting cathodes. DMEM contained phenol red, which colored the surroundings of the electrodes in yellow (around the anode) and pink (around the cathode) due to pH change. We also observed gas bubbles. These signs were mild with a single treatment, but much noticeable with two consecutive trains. Additionally, we monitored the applied voltage and the electric current. No significant changes were observed in any treatment.

## IV. DISCUSSION

According to the obtained results, and as expected, treatment overlap can substantially increase irreversible electroporation damage. Cell death rises when two high electric field treatments were sequentially applied.

It is known that a higher number of pulses reduces the irreversible electric field threshold, which tends to saturate at around 70 to 100 pulses [27]. In the 10 pulse protocols, the saturation point was not reached, as we observed that a second train reduced cell viability. Instead, with the 100 pulse protocol, the second train did not add to cell death.

Another factor which reduces the electric field threshold is inter-pulse pause. It has been reported that cell membrane needs from seconds to a few minutes to recover from electroporation. However, if a pulse is applied before the membrane has fully recovered, the membrane is further electroporated [18]. Although we were studying the pause between two trains (instead of pulses), the general effect also applies. This explains why lower survival probabilities were found with the 10 s pause compared to 1 minute pause.

Interestingly, the order of the treatments (i.e., whether the higher field treatment is first or second) did not produce observable differences in the outcome. Yao et al. [44] found that applying short high voltage pulses (a few kV/cm for a couple of microseconds) before a standard 80 NTIRE pulses generated a larger ablation area than with the standard NTIRE protocol on potato tuber. Pulsing the other way around did not increase the treated area. The voltage to distance ratios they used for the high pulses were of the order of 3-4 kV/cm, which were up to 10 times larger than the low fields. In our study, we did not surpass 1.5 kV/cm for the high pulses, and proportionally the low electric fields were not as low (25% ratio). These lower fields could explain why we did not observe any difference between $H+L$ and $L+H$ protocols, i.e., the order of the overlapping fields did not add to cell death.

Three different methods were compared to predict cell death in overlapping treatments: A) the geometrical union of the individual treatments, B) the method proposed by Garcia et al. [31] in which the overall treatment is obtained by multiplying the fields of probability of cell survival from the individual treatments, and C) our adapted logistic model of overlapping treatments. We computed precision (5), miss rate (6) and Dice (7) metrics, after classifying the state of the cell with a threshold of 851 V/cm (IRE threshold) for method A, and a 5 % cell survival probability for methods B and C. A precision of 1 indicates that the predicted treatment region contains only dead cells, whereas lower values reveal the proportion of remaining living cells. In this regard, we found that all the methods perform equally well, with a precision ≥ 0.982 and a maximum difference of only 0.4 percent points. On the other hand, the miss rate revealed differences between the methods. This metric represents the proportion of dead cells that fall outside the treatment region. Higher scores indicate a larger transition of living/dead cells. In this case, we
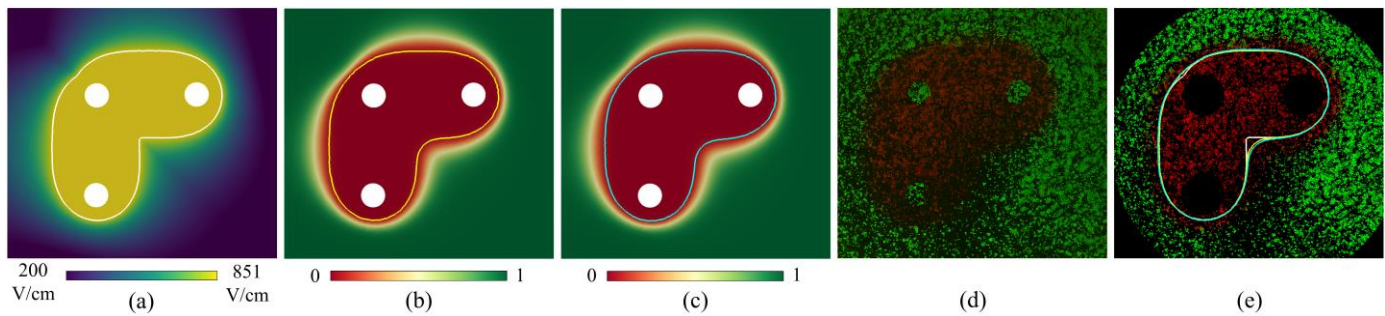
Fig. 7. Predicted treated area with the three analyzed methods for a protocol of two trains of 10 pulses at 600 V, 1 minute pause. (a) electric field distribution (white contour at the irreversible electric field threshold of 851 V/cm). (b) probability of survival of the product of individual pairs (yellow contour at 95% cell death). (c) probability of survival of the adapted logistic model of overlapping electric fields (cyan contour at 95% cell death). (d): original image with calcein AM in the green channel (living cells) and PI in the red channel (dead cells) (e): segmentation of the ROI with an overlay of the isocontours at the defined critical values for the three methods (same colors as in (a), (b) and (c)).

found that methods B and C perform slightly better than the electric field threshold criterion (1.2 to 4.3 percent points lower), with C marginally outperforming B by up to 3.1 points. This reduction in miss rate is also reflected in the Dice score. In addition, the AUC metric reveals how accurate a classifier is regardless of the threshold. It confirms that all the methods perform great (AUC > 0.961), with method B and C taking the lead by a minimal margin.

These slight improvements can be graphically understood by observing the shape of the ablation area that our 2D setup generated (L-shaped). It can be seen in Fig. 7.e that the isocontour provided by the electric field threshold criterion (method A) presents a sharp angled corner, whereas that same corner is smoother with the other two methods. Despite the slight accuracy improvements offered by methods B and C, these results suggest that, considering other sources of uncertainty typically present in electroporation treatment (e.g., placement of the electrodes), overall, the electric field threshold method can be considered as accurate as the probabilistic models in predicting the treatment region.

This suggests that for NTIRE procedures, which typically apply between 70 and 100 pulses per pair, treatment overlap does not play a significant role (we only observed an increase in cell death with overlapping treatments with 10 pulse protocols, and not with 100 pulses). However, this study only contemplated two overlapping pulse trains, contrary to actual procedures which can present more overlapping treatments, although marginal differences can be presumed.

On the other hand, ECT aims to reversibly electroporate the tissue so the therapeutic drug can penetrate into the cells, but it is not uncommon to find damage due to IRE near the electrodes. Due to the lower pulse count per train (8 to 10 pulses), overlapping treatments can slightly enlarge the irreversibly treated tissue around the electrodes, according to our results. This can be further confirmed by some preliminary 3D simulations, where the predicted IRE lesion volume was increased by 13.7 ± 5.5 % (average ± standard deviation) with B, and up to 22.9 ± 8.6 % with C when compared to A. (See Table s.IV and Figs. s.2 to s.4 in the supplementary materials).

It must be pointed out that the modeling methods do not fit the validation data as well as they fit the characterization data. In the 1D setup, the reduced cell viability due to overlapping fields follows a curved shape (Fig. 5), but that shape appears straighter when looking at the data from the validation phase (Fig. 6). Although this effect can be partially accounted by experimental uncertainty (we are reporting a 3SE interval of around ±30 V/cm), this effect could also be a consequence of the highly different electric field distributions between the two setups. While in the characterization assays the electric field in the two treatments had the same direction, in the validation setup we applied two fields at different angles (up to 90 degrees). Membrane polarization mostly occurs at the surfaces which are perpendicular to the electric field [45]. This implies that in the 1D setup the cell membrane was always polarized in the same region. Instead, in the 2D assays, the first and second trains polarized the membrane in different directions. Thus, there was a larger polarized area in the 2D setup. This suggests that cells in the validation setup presented a larger electroporated membrane area [46], which could add to cell death.

Another limitation of the assays is that cell death does not reach 100%, even well above the electric field threshold (Fig. 6). This is reflected in the precision metric where no method surpasses 97.5%. In some images, we observed noise speckles in the calcein AM channel. We filtered the cells by size, but some of the noise bypassed it. We also observed living cells within the ablation zone in most of the images. However, such cells were no longer adhered to the well surface. It is likely that these cells were still in an apoptotic process after the 3-hour period we analyzed. It has been reported that 24 hours is a better interval for evaluating apoptosis due to IRE [47]–[49], but we found in preliminary assays that cell proliferation overtook the treatment zone after 24 hours.

Finally, the present study is not considering the possible impact of conductivity changes caused by electroporation. In the cell models used here the conductivity changes due to electroporation are likely to be negligible as the thin layer of cells is embedded in a relatively much bulkier ionic medium. However, it has been demonstrated that in tissues, where cells are densely packed, the conductivity changes caused by electroporation can have a substantial impact on the electric field distribution and hence on the TV [50]. Therefore, for thoroughly studying treatment overlap, it would be judicious to analyze the impact on field distribution that preceding treatments can have on subsequent treatments due to conductivity changes caused by electroporation. (Sophisticated mathematical constructs have been proposed to model such effect [51]–[57].) Nevertheless, it must be taken into account that whereas conductivity changes within each

pulse (in-pulse conductivity) can be very high (and that is why they can have a significant impact on the field distribution), this in-pulse conductivity is only slightly influenced by the preceding pulses or sequences of pulses [58]. In preliminary simulations reported in the supplementary materials where we coarsely approximated this effect considering worst-case assumptions, we found minimal consequences (<1.36 % difference). Therefore, we conclude that the impact of conductivity changes does not modify the qualitative conclusions reached here.

## V. Conclusions

Treatment overlap is present in almost every electroporation procedure but, to the best of our knowledge, its impact had not yet been quantified. We found that, as expected, overlapping treatments can substantially reduce the electric field threshold needed to induce cell death and thus increase the efficacy of the overall treatment. However, in terms of TV, we deduce that the impact of overlapping treatments will be minor in typical NTIRE procedures in which trains of 70 or more pulses are applied through multiple electrode pairs. Importantly, the overall ablation volume will be predicted with a reasonable level of accuracy by simply performing the geometric union of the ablation volumes predicted for each electrode pair. Although this study did not evaluate treatment overlap *in vivo*, we presume that the method used in most NTIRE pre-clinical and clinical studies is adequate. We also confirmed that the model proposed by Garcia et al., [31] is valid for predicting treatment overlap, as well as the adapted logistic model introduced here. At last, even if this study does not explicitly contemplate ECT, it can be inferred that the same general conclusions apply to treatment overlap in ECT procedures.

## References

[1] J. C. Weaver and Y. A. Chizmadzhev, "Theory of electroporation: A review," *Bioelectrochemistry Bioenerg.*, vol. 41, no. 2, pp. 135–160, Dec. 1996.

[2] D. Miklavcic et al., "In vivo electroporation threshold determination," in *Annual International Conference of the IEEE Engineering in Medicine and Biology - Proceedings*, 2000, vol. 4, pp. 2815–2818.

[3] L. M. Mir et al., "Effective treatment of cutaneous and subcutaneous malignant tumours by electrochemotherapy," *Br. J. Cancer*, vol. 77, no. 12, pp. 2336–2342, Jun. 1998.

[4] G. Sersa et al., "Electrochemotherapy in treatment of tumours," *Eur. J. Surg. Oncol.*, vol. 34, no. 2, pp. 232–240, Feb. 2008.

[5] T. Garcia-Sanchez et al., "Successful Tumor Electrochemotherapy Using Sine Waves," *IEEE Trans. Biomed. Eng.*, vol. 67, no. 4, pp. 1040–1049, Apr. 2020.

[6] R. V. Davalos et al., "Tissue ablation with irreversible electroporation," *Ann. Biomed. Eng.*, vol. 33, no. 2, pp. 223–231, Feb. 2005.

[7] B. Rubinsky, "Irreversible Electroporation in Medicine," *Technol. Cancer Res. Treat.*, vol. 6, no. 4, pp. 255–259, Aug. 2007.

[8] A.-C. Durieux et al., "In vivo gene electrotransfer into skeletal muscle: effects of plasmid DNA on the occurrence and extent of muscle damage," *J. Gene Med.*, vol. 6, no. 7, pp. 809–816, Jul. 2004.

[9] A. Gothelf and J. Gehl, "Gene Electrotransfer to Skin; Review of Existing Literature and Clinical Perspectives," *Curr. Gene Ther.*, vol. 10, no. 4, pp. 287–299, Jul. 2010.

[10] A. Sugrue et al., "Irreversible electroporation for the treatment of cardiac arrhythmias," *Expert Review of Cardiovascular Therapy*, vol. 16, no. 5. Taylor and Francis Ltd, pp. 349–360, May 04, 2018.

[11] R. Van Es et al., "High-frequency irreversible electroporation for cardiac ablation using an asymmetrical waveform," *Biomed. Eng. Online*, vol. 18, no. 1, pp. 1–13, Jun. 2019.

[12] L. P. Beyer and P. Wiggermann, "Treatment Planning, Needle Insertion, Image Guidance, and Endpoint Assessment," in *Irreversible Electroporation in Clinical Practice*, Cham: Springer International Publishing, 2018, pp. 115–120.

[13] A. Zupanic et al., "Treatment planning of electroporation-based medical interventions: Electrochemotherapy, gene electrotransfer and irreversible electroporation," *Phys. Med. Biol.*, vol. 57, no. 17, pp. 5425–5440, Sep. 2012.

[14] J. F. Edd et al., "In vivo results of a new focal tissue ablation technique: Irreversible electroporation," *IEEE Trans. Biomed. Eng.*, vol. 53, no. 7, pp. 1409–1415, Jul. 2006.

[15] D. Miklavčič et al., "A validated model of in vivo electric field distribution in tissues for electrochemotherapy and for DNA electrotransfer for gene therapy," *Biochim. Biophys. Acta - Gen. Subj.*, vol. 1523, no. 1, pp. 73–83, Sep. 2000.

[16] D. Miklavčič et al., "The importance of electric field distribution for effective in vivo electroporation of tissues," *Biophys. J.*, vol. 74, no. 5, pp. 2152–2158, May 1998.

[17] G. Saulis and R. Saule, "Comparison of electroporation threshold for different cell lines in vitro," in *Acta Physica Polonica A*, 2009, vol. 115, no. 6, pp. 1056–1058.

[18] A. M. Lebar et al., "Inter-pulse interval between rectangular voltage pulses affects electroporation threshold of artificial lipid bilayers," *IEEE Trans. Nanobioscience*, vol. 1, no. 3, pp. 116–120, 2002.

[19] E. Perera-Bel et al., "EView: An electric field visualization web platform for electroporation-based therapies," *Comput. Methods Programs Biomed.*, vol. 197, p. 105682, Dec. 2020.

[20] J. F. Edd and R. V. Davalos, "Mathematical Modeling of Irreversible Electroporation for Treatment Planning," *Technol. Cancer Res. Treat.*, vol. 6, no. 4, pp. 275–286, Aug. 2007.

[21] D. Pavliha et al., "Patient-specific treatment planning of electrochemotherapy: Procedure design and possible pitfalls," *Bioelectrochemistry*, vol. 87, pp. 265–273, Oct. 2012.

[22] P. A. Garcia et al., "Intracranial nonthermal irreversible electroporation: In vivo analysis," *J. Membr. Biol.*, vol. 236, no. 1, pp. 127–136, Jul. 2010.

[23] D. Miklavcic et al., "Towards treatment planning and treatment of deep-seated solid tumors by electrochemotherapy," *Biomed. Eng. Online*, vol. 9, no. 1, pp. 1–12, Feb. 2010.

[24] R. E. Neal and R. V. Davalos, "The feasibility of irreversible electroporation for the treatment of breast cancer and other heterogeneous systems," *Ann. Biomed. Eng.*, vol. 37, no. 12, pp. 2615–2625, Dec. 2009.

[25] B. Kos et al., "Careful treatment planning enables safe ablation of liver tumors adjacent to major blood vessels by percutaneous irreversible electroporation (IRE)," *Radiol. Oncol.*, vol. 49, no. 3, pp. 234–241, 2015.

[26] O. Gallinato et al., "Numerical workflow of irreversible electroporation for deep-seated tumor," *Phys. Med. Biol.*, vol. 64, no. 5, p. 055016, Mar. 2019.

[27] J. Dermol and D. Miklavčič, "Mathematical Models Describing Chinese Hamster Ovary Cell Death Due to Electroporation In Vitro," *J. Membr. Biol.*, vol. 248, no. 5, pp. 865–881, Oct. 2015.

[28] M. P. Rols and J. Teissié, "Electropermeabilization of mammalian cells to macromolecules: Control by pulse duration," *Biophys. J.*, vol. 75, no. 3, pp. 1415–1423, Sep. 1998.

[29] G. Pucihar et al., "Equivalent pulse parameters for electroporation," *IEEE Trans. Biomed. Eng.*, vol. 58, no. 11, pp. 3279–3288, Nov. 2011.

[30] S. Campelo et al., "An evaluation of irreversible electroporation thresholds in human prostate cancer and potential correlations to physiological measurements," *APL Bioeng.*, vol. 1, no. 1, p. 016101, Dec. 2017.

[31] P. A. Garcia et al., "Predictive therapeutic planning for irreversible electroporation treatment of spontaneous malignant glioma," *Med. Phys.*, vol. 44, no. 9, pp. 4968–4980, Sep. 2017.

[32] A. Golberg and B. Rubinsky, "A statistical model for multidimensional irreversible electroporation cell death in tissue," *Biomed. Eng. Online*, vol. 9, no. 1, p. 13, Feb. 2010.

[33] L. Ding et al., "Treatment Planning Optimization in Irreversible Electroporation for Complete Ablation of Variously Sized Cervical Tumors: A Numerical Study," *J. Biomech. Eng.*, vol. 143, no. 1,

Jan. 2021.

[34] S. Sharabi *et al.*, "A statistical model describing combined irreversible electroporation and electroporation-induced blood-brain barrier disruption," *Radiol. Oncol.*, 2016.

[35] Y. Yang *et al.*, "Development of a statistical model for cervical cancer cell death with irreversible electroporation in vitro," *PLoS One*, vol. 13, no. 4, p. e0195561, Apr. 2018.

[36] J. Schindelin *et al.*, "Fiji: An open-source platform for biological-image analysis," *Nature Methods*, vol. 9, no. 7. Nature Publishing Group, pp. 676–682, Jul. 28, 2012.

[37] C. A. Schneider *et al.*, "NIH Image to ImageJ: 25 years of image analysis," *Nature Methods*, vol. 9, no. 7. Nature Publishing Group, pp. 671–675, Jul. 28, 2012.

[38] B. Sankur, "Survey over image thresholding techniques and quantitative performance evaluation," *J. Electron. Imaging*, vol. 13, no. 1, p. 146, Jan. 2004.

[39] J. Bernsen, "Dynamic Thresholding of Gray Level Image," in *Proceedings of International Conference on Pattern Recognition*, 1986, pp. 1251–1255.

[40] M. Wilkinson, "Automated and manual segmentation techniques in image analysis of microbes," in *Digital Image Analysis of Microbes: Imaging, Morphometry, Fluorometry and Motility Techniques and Applications*, John Wiley & Sons, 1998.

[41] R Core Team, "R: A Language and Environment for Statistical Computing." Vienna, Austria, 2021.

[42] A. J. Dobson and A. G. Barnett, *An introduction to generalized linear models*. CRC press, 2018.

[43] A. A. Taha and A. Hanbury, "Metrics for evaluating 3D medical image segmentation: Analysis, selection, and tool," *BMC Med. Imaging*, vol. 15, no. 1, p. 29, Aug. 2015.

[44] C. Yao *et al.*, "Irreversible electroporation ablation area enhanced by synergistic high- and low-voltage pulses," *PLoS One*, vol. 12, no. 3, p. e0173181, Mar. 2017.

[45] P. Marszalek *et al.*, "Schwan equation and transmembrane potential induced by alternating electric field," *Biophys. J.*, vol. 58, no. 4, pp. 1053–1058, Oct. 1990.

[46] B. Gabriel and J. Teissié, "Direct observation in the millisecond time range of fluorescent molecule asymmetrical interaction with the electropermeabilized cell membrane," *Biophys. J.*, vol. 73, no. 5, pp. 2630–2637, Nov. 1997.

[47] H. B. Kim *et al.*, "Changes of apoptosis in tumor tissues with time after irreversible electroporation," *Biochem. Biophys. Res. Commun.*, vol. 435, no. 4, pp. 651–656, Jun. 2013.

[48] Y. Guo *et al.*, "Irreversible electroporation therapy in the liver: Longitudinal efficacy studies in a rat model of hepatocellular carcinoma," *Cancer Res.*, vol. 70, no. 4, pp. 1555–1563, Feb. 2010.

[49] B. Mercadal *et al.*, "Dynamics of Cell Death After Conventional IRE and H-FIRE Treatments," *Ann. Biomed. Eng.*, vol. 48, no. 5, pp. 1451–1462, May 2020.

[50] A. Ivorra *et al.*, "Electric Field Redistribution due to Conductivity Changes during Tissue Electroporation: Experiments with a Simple Vegetal Model," in *IFMBE Proceedings*, vol. 25, no. 13, Springer, Berlin, Heidelberg, 2009, pp. 59–62.

[51] R. Weinert *et al.*, "Inclusion of memory effects in a dynamic model of electroporation in biological tissues," *Artif. Organs*, vol. 43, no. 7, pp. 688–693, Jul. 2019.

[52] A. Ramos and R. L. Weinert, "Mathematical and computational method for electrical analysis of biological tissues," *J. Comput. Electron.*, vol. 17, no. 1, pp. 382–391, Mar. 2018.

[53] D. Voyer *et al.*, "Dynamical modeling of tissue electroporation," *Bioelectrochemistry*, vol. 119, pp. 98–110, Feb. 2018.

[54] M. Leguèbe *et al.*, "Conducting and permeable states of cell membrane submitted to high voltage pulses: Mathematical and numerical studies validated by the experiments," *J. Theor. Biol.*, vol. 360, pp. 83–94, Nov. 2014.

[55] J. Langus *et al.*, "Dynamic finite-element model for efficient modelling of electric currents in electroporated tissue," *Sci. Rep.*, vol. 6, no. 1, p. 26409, Sep. 2016.

[56] E. Luján *et al.*, "Towards an optimal dose-response relationship in gene electrotransfer protocols," *Electrochim. Acta*, vol. 319, pp. 1002–1011, Oct. 2019.

[57] M. Marino *et al.*, "OpenEP : an open-source simulator for electroporation-based tumor treatments," *Sci. Reports 2021 111*, vol. 11, no. 1, pp. 1–15, Jan. 2021.

[58] A. Ivorra, "Tissue Electroporation as a Bioelectric Phenomenon: Basic Concepts," Springer, Berlin, Heidelberg, 2010, pp. 23–61.

# Supplementary material

- **Equivalence between the Peleg-Fermi model and the logistic regression**

The Peleg-Fermi equation is used to describe cell survival probability in irreversible electroporation as a function of the electric field magnitude and the number of applied pulses [1]. The probability of survival of a pulse train ($S$) is defined as:

$$S = \frac{1}{1 + e^{\frac{E - E_C(n)}{A(n)}}} \qquad (s.1)$$

where $E$ is the electric field magnitude, $E_C(n)$ is the electric field at which $S = 0.5$, and $A(n)$ is the factor which determines the slope of the transition of the curve. $E_C$ and $A$ are exponential decay functions dependent on the number of pulses $n$.

$$E_c(n) = E_{c0} \cdot e^{-k_1 n} \qquad (s.2)$$

$$A(n) = A_0 \cdot e^{-k_2 n} \qquad (s.3)$$

$E_C$ describes the critical electric field at which 50% of cells are dead, with $E_{c0}$ being its initial magnitude and $k_1$ its exponential decay coefficient. $A$ determines the transition from living to dead cells, with an initial value $A_0$ and a decay coefficient $k_2$.

In the present study we evaluated each protocol independently, thus, ignoring the dependence on the number of pulses. $E_C$ and $A$ become constants and equation (s.1) is rewritten as:

$$S = \frac{1}{1 + e^{\frac{E - E_C}{A}}} \qquad (s.4)$$

This equation is, in fact, a logistic model, where the exponential term can be rewritten as a first-degree polynomial.

$$S = \frac{1}{1 + e^{-(\beta_0 + \beta_1 E)}} \qquad (s.5)$$

where $\beta_0$ is the intercept and $\beta_1$ is the slope of the polynomial. The equivalence between the Peleg-Fermi model (s.4) and the logistic regression (s.5) is obtained by:

$$\beta_0 = \frac{E_c}{A} \qquad (s.6)$$

$$\beta_1 = \frac{-1}{A} \qquad (s.7)$$

- **Fitting parameters of the logistic regressions**

TABLE s.I
FITTING PARAMETERS OF THE LOGISTIC REGRESSION FOR THE $H+L$ AND $L+H$ PROTOCOLS (EQUATION 1).
THE PARAMETERS OF METHOD B ARE THE ONES FROM A SINGLE TREATMENT (I.E., 100% + 0%)

| Pulses | Period | Voltage strength | $\beta_0$ Value | $\beta_0$ ±3SE | | $\beta_1$ Value | $\beta_1$ ±3SE | |
|---|---|---|---|---|---|---|---|---|
| | | 100% + 0% | 9.913 | 9.782 | 10.046 | $-1.51 \cdot 10^{-2}$ | $-1.53 \cdot 10^{-2}$ | $-1.49 \cdot 10^{-2}$ |
| | | 100% + 25% | 9.409 | 9.204 | 9.617 | $-1.41 \cdot 10^{-2}$ | $-1.44 \cdot 10^{-2}$ | $-1.38 \cdot 10^{-2}$ |
| | | 100% + 50% | 10.895 | 10.663 | 11.131 | $-1.71 \cdot 10^{-2}$ | $-1.75 \cdot 10^{-2}$ | $-1.68 \cdot 10^{-2}$ |
| | | 100% + 75% | 9.435 | 9.244 | 9.627 | $-1.57 \cdot 10^{-2}$ | $-1.60 \cdot 10^{-2}$ | $-1.53 \cdot 10^{-2}$ |
| | 10 s | 100% + 100% | 10.204 | 10.002 | 10.410 | $-1.85 \cdot 10^{-2}$ | $-1.89 \cdot 10^{-2}$ | $-1.81 \cdot 10^{-2}$ |
| | | 100% + 0% | 9.913 | 9.782 | 10.046 | $-1.51 \cdot 10^{-2}$ | $-1.53 \cdot 10^{-2}$ | $-1.49 \cdot 10^{-2}$ |
| | | 25% + 100% | 9.746 | 9.543 | 9.952 | $-1.50 \cdot 10^{-2}$ | $-1.54 \cdot 10^{-2}$ | $-1.47 \cdot 10^{-2}$ |
| | | 50% + 100% | 9.438 | 9.245 | 9.633 | $-1.46 \cdot 10^{-2}$ | $-1.50 \cdot 10^{-2}$ | $-1.43 \cdot 10^{-2}$ |
| 10 | | 75% + 100% | 9.759 | 9.563 | 9.958 | $-1.60 \cdot 10^{-2}$ | $-1.63 \cdot 10^{-2}$ | $-1.56 \cdot 10^{-2}$ |
| + | | 100% + 100% | 10.204 | 10.002 | 10.410 | $-1.85 \cdot 10^{-2}$ | $-1.89 \cdot 10^{-2}$ | $-1.81 \cdot 10^{-2}$ |
| 10 | | 100% + 0% | 9.913 | 9.782 | 10.046 | $-1.51 \cdot 10^{-2}$ | $-1.53 \cdot 10^{-2}$ | $-1.49 \cdot 10^{-2}$ |
| | | 100% + 25% | 10.327 | 10.113 | 10.544 | $-1.58 \cdot 10^{-2}$ | $-1.62 \cdot 10^{-2}$ | $-1.55 \cdot 10^{-2}$ |
| | | 100% + 50% | 10.493 | 10.263 | 10.727 | $-1.67 \cdot 10^{-2}$ | $-1.70 \cdot 10^{-2}$ | $-1.63 \cdot 10^{-2}$ |
| | | 100% + 75% | 9.863 | 9.638 | 10.091 | $-1.60 \cdot 10^{-2}$ | $-1.63 \cdot 10^{-2}$ | $-1.56 \cdot 10^{-2}$ |
| | 1 min | 100% + 100% | 9.795 | 9.625 | 9.968 | $-1.65 \cdot 10^{-2}$ | $-1.68 \cdot 10^{-2}$ | $-1.62 \cdot 10^{-2}$ |
| | | 100% + 0% | 9.913 | 9.782 | 10.046 | $-1.51 \cdot 10^{-2}$ | $-1.53 \cdot 10^{-2}$ | $-1.49 \cdot 10^{-2}$ |
| | | 25% + 100% | 10.673 | 10.473 | 10.876 | $-1.69 \cdot 10^{-2}$ | $-1.73 \cdot 10^{-2}$ | $-1.66 \cdot 10^{-2}$ |
| | | 50% + 100% | 9.764 | 9.578 | 9.952 | $-1.56 \cdot 10^{-2}$ | $-1.59 \cdot 10^{-2}$ | $-1.53 \cdot 10^{-2}$ |
| | | 75% + 100% | 10.189 | 9.992 | 10.389 | $-1.58 \cdot 10^{-2}$ | $-1.61 \cdot 10^{-2}$ | $-1.55 \cdot 10^{-2}$ |
| | | 100% + 100% | 9.795 | 9.625 | 9.968 | $-1.65 \cdot 10^{-2}$ | $-1.68 \cdot 10^{-2}$ | $-1.62 \cdot 10^{-2}$ |
| 100 | - | 100% + 0% | 7.087 | 6.970 | 7.206 | $-1.64 \cdot 10^{-2}$ | $-1.66 \cdot 10^{-2}$ | $-1.61 \cdot 10^{-2}$ |
| + | 10 s | 100% + 100% | 6.599 | 6.485 | 6.714 | $-1.57 \cdot 10^{-2}$ | $-1.60 \cdot 10^{-2}$ | $-1.55 \cdot 10^{-2}$ |
| 100 | 1 min | 100% + 100% | 6.679 | 6.559 | 6.801 | $-1.55 \cdot 10^{-2}$ | $-1.58 \cdot 10^{-2}$ | $-1.52 \cdot 10^{-2}$ |

TABLE s.II
FITTING PARAMETERS OF THE ADAPTED LOGISTIC REGRESSION OF OVERLAPPING PAIRS (METHOD C) (EQUATION 4)

| Protocol | $\beta_0$ Value | $\beta_0$ ±3SE | | $\beta_1$ Value | $\beta_1$ ±3SE | | $\beta_2$ Value | $\beta_2$ ±3SE | |
|---|---|---|---|---|---|---|---|---|---|
| 10 + 10, 10 s | 9.648 | 9.461 | 9.835 | $-1.47 \cdot 10^{-2}$ | $-1.50 \cdot 10^{-2}$ | $-1.44 \cdot 10^{-2}$ | $-1.10 \cdot 10^{-3}$ | $-1.20 \cdot 10^{-3}$ | $-1.00 \cdot 10^{-3}$ |
| 10 + 10, 1min | 9.919 | 9.732 | 10.105 | $-1.53 \cdot 10^{-2}$ | $-1.56 \cdot 10^{-2}$ | $-1.50 \cdot 10^{-2}$ | $-2.00 \cdot 10^{-4}$ | $-2.90 \cdot 10^{-4}$ | $-1.11 \cdot 10^{-4}$ |

- **Predicted treatment volume for electrode configurations typically used in actual electroporation-based treatments**

We performed some preliminary 3D simulations to extrapolate the findings of the 2D cell culture assays to scenarios closer resembling actual electroporation-based treatments. We compared the predictive accuracy in overlapping treatments of the three studied methodologies for 10-pulse treatments. Three electrode configurations typically used in electroporation-based treatments, and in particular in NTIRE procedures, were simulated, and the ablated volume (irreversibly electroporated) was obtained. Three setups were considered: 4-SQ) four electrodes in a square pattern at 15 mm separation, 20 mm length and 1 mm diameter, 6-RECT): two parallel lines of three electrodes in parallel (forming a rectangle) at 15 mm separation, 20 mm length and 1 mm diameter, and 7-HEX) six electrodes forming a hexagon with one electrode in the center at 7.3 mm separation, 20 mm length and 0.7 mm diameter.

Two voltage to distance ratios were considered for the treatments: 1000 V/cm and 1500 V/cm between active electrodes. We limited the voltage to 3000 V, which is the maximum in most commercial generators. See the simulated voltages in table s.III.

TABLE s.III
SIMULATED VOLTAGES

| | Voltage/distance ratio (V/cm) | Voltage (V) | |
| --- | --- | --- | --- |
| | | In-line pairs | Diagonal pairs |
| 4-SQ | 1000 | 1500 | 2121 |
| | 1500 | 2250 | 3000 |
| 6-RECT | 1000 | 1500 | 2121 |
| | 1500 | 2250 | 3000 |
| 7-HEX | 1000 | 730 | |
| | 1500 | 1095 | |

As in the case of tissues it has been demonstrated that electrical conductivity changes caused by electroporation can have a substantial impact on the electric field distribution and hence on the treatment volume, here, for higher verisimilitude, the simulation was performed on a 3D homogeneous domain assuming a non-linear electrical conductivity. The conductivity profile followed a symmetric sigmoid function and had been fit to *ex vivo* porcine liver data [2], [3].

$$\sigma(E) = \sigma_0 + \frac{\sigma_f - \sigma_0}{1 + A \cdot e^{\left(-\frac{|E|-B}{C}\right)}} \tag{s.8}$$

where $E$ is the electric field magnitude and $\sigma_0$ is the (static) conductivity when no electric field is applied (0.188 S/m), $\sigma_f$ is the maximum conductivity that can be reached during electroporation (0.289 S/m), and $A$ (80.03), $B$ (613.1 V/cm) and $C$ (252.2 V/cm) are shape parameters.

The IRE volume was predicted using the three studied methodologies: A) the geometrical union of the individual treatments, B) the method in which the overall treatment is obtained by multiplying the fields of probability of cell survival from the individual treatments, and C) our adapted logistic model of overlapping treatments. For method A, an electric field threshold of 851 V/cm was used (corresponding to 95 % of cell death of a single treatment of 10 pulses). For methods B and C, the ablated volume was set to be that which has a survival probability of 5% or lower. Because method C was calibrated only for two overlapping treatments, the survival probability was only computed using the two trains that generated the highest electric fields (at each mesh node).

Notice that the survival probability curves and electric field threshold have been obtained from the assays on CHO cells performed in this study. The fact that we use a non-linear conductivity of porcine liver is just to represent the effect of this parameter on the predicted treatment volume. Hence, the treated volume shapes represented here do not correspond to actual treatments.

The predicted volumes are reported in table s.IV and are displayed in Figs. s.2 to s.4.

- **Impact on field distribution that preceding treatments can have on subsequent treatments due to conductivity changes caused by electroporation**

In addition to simulating the in-pulse conductivity, we modeled the static conductivity to be influenced by the preceding pulses. It has been observed that after a sequence of pulses, the static conductivity is larger than it was before the treatment [4]. This phenomenon has not been previously modelled, but, as an extreme upper bound to this effect, we defined the static conductivity ($\sigma_{0,i}$) to be the average between $\sigma_0$ and the previous pair conductivity $\sigma_{i-1}(E)$. Notice that this is an extreme assumption, thus, the effect in real scenarios should be much lower. Equation (s.8) is then modified:

$$\sigma_i(E) = \sigma_{0,i} + \frac{\sigma_f - \sigma_{0,i}}{1 + A \cdot e^{\left(-\frac{|E|-B}{C}\right)}}$$

$$\sigma_{0,i} = \frac{\sigma_0 + \sigma_{i-1}(E)}{2}$$

(s. 9)

The predicted volumes are reported in table s.IV (see "Conductivity equation" column) and are displayed in Fig. s.5.

TABLE s.IV
PREDICTED TREATMENT VOLUME WITH THE THREE STUDIED METHODS
FOR THE DIFFERENT ELECTRODE CONFIGURATIONS AND PULSING PARAMETERS

| Electrode configuration | Voltage/distance ratio (V/cm) | Conductivity equation | Predicted TV (cm$^3$) | | | |
|---|---|---|---|---|---|---|
| | | | A | B | C (1 minute) | C (10 s) |
| 4-SQ | 1000 | (s.8) | 4.80 | 5.27 | 5.44 | 5.85 |
| | | (s.9) | 4.82 | 5.29 | 5.46 | 5.88 |
| | 1500 | (s.8) | 10.77 | 12.32 | 12.51 | 13.17 |
| | | (s.9) | 10.79 | 12.34 | 12.53 | 13.20 |
| 6-RECT | 1000 | (s.8) | 7.42 | 8.52 | 8.63 | 9.32 |
| | | (s.9) | 7.44 | 8.56 | 8.67 | 9.36 |
| | 1500 | (s.8) | 17.03 | 20.00 | 20.11 | 21.17 |
| | | (s.9) | 17.06 | 20.04 | 20.14 | 21.20 |
| 7-HEX | 1000 | (s.8) | 1.69 | 2.04 | 2.08 | 2.29 |
| | | (s.9) | 1.71 | 2.07 | 2.11 | 2.32 |
| | 1500 | (s.8) | 5.10 | 5.34 | 5.35 | 5.50 |
| | | (s.9) | 5.12 | 5.35 | 5.37 | 5.51 |

(a)  (b)  (c)

(d)  (e)  (f)
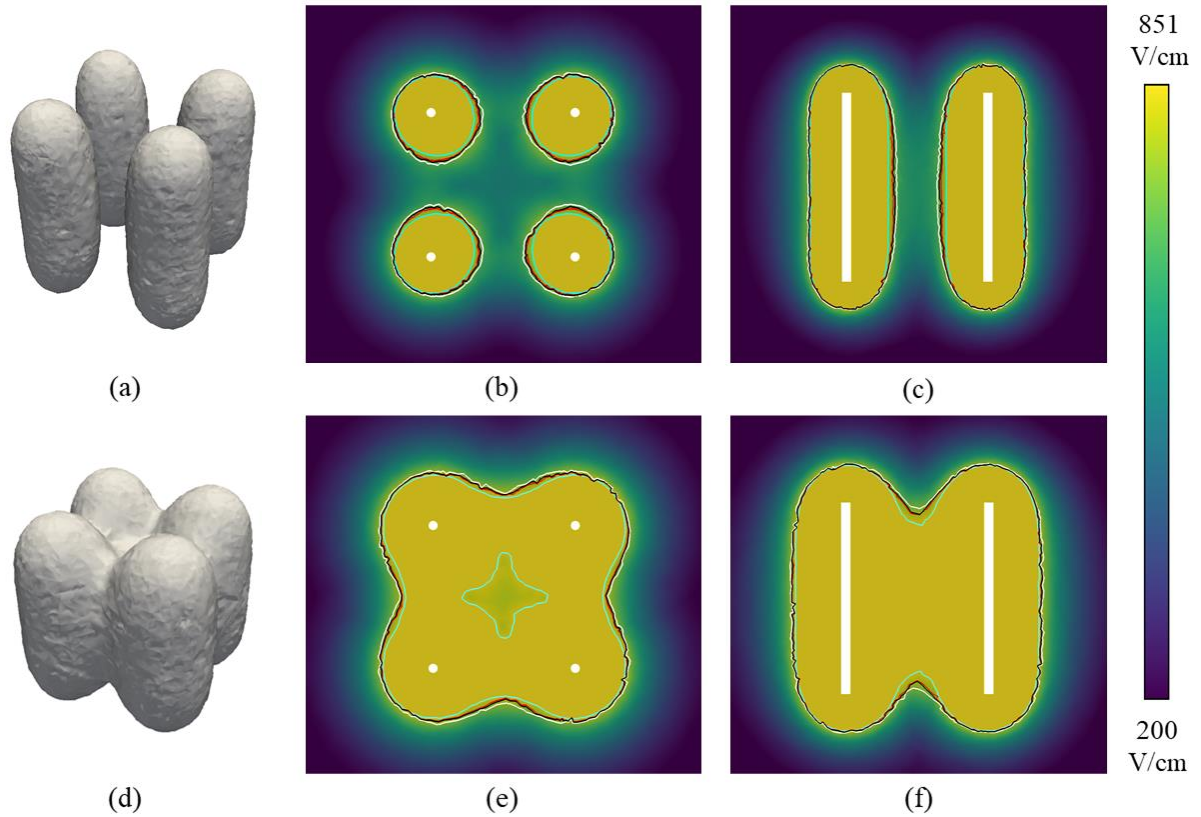
Fig. s.2. Predicted ablated volume in the 4-SQ setup. Electrode spacing is 15 mm and the diameter is 1 mm. (a), (b), and (c) correspond to the treatment at 1000 V/cm voltage to distance ratio, and (d), (e), and (f) correspond to 1500 V/cm one. (a) and (d) display the predicted volume for method C at 10 s inter-treatment pause. (b) and (e) are the transversal cross section and (c) and (f) are the longitudinal cross section with the simulated electric field distribution. The contours correspond to the predicted TV for method A (cyan), method B (red), method C for 1 min inter-treatment pause (black), and method C for 10 s pause (white).
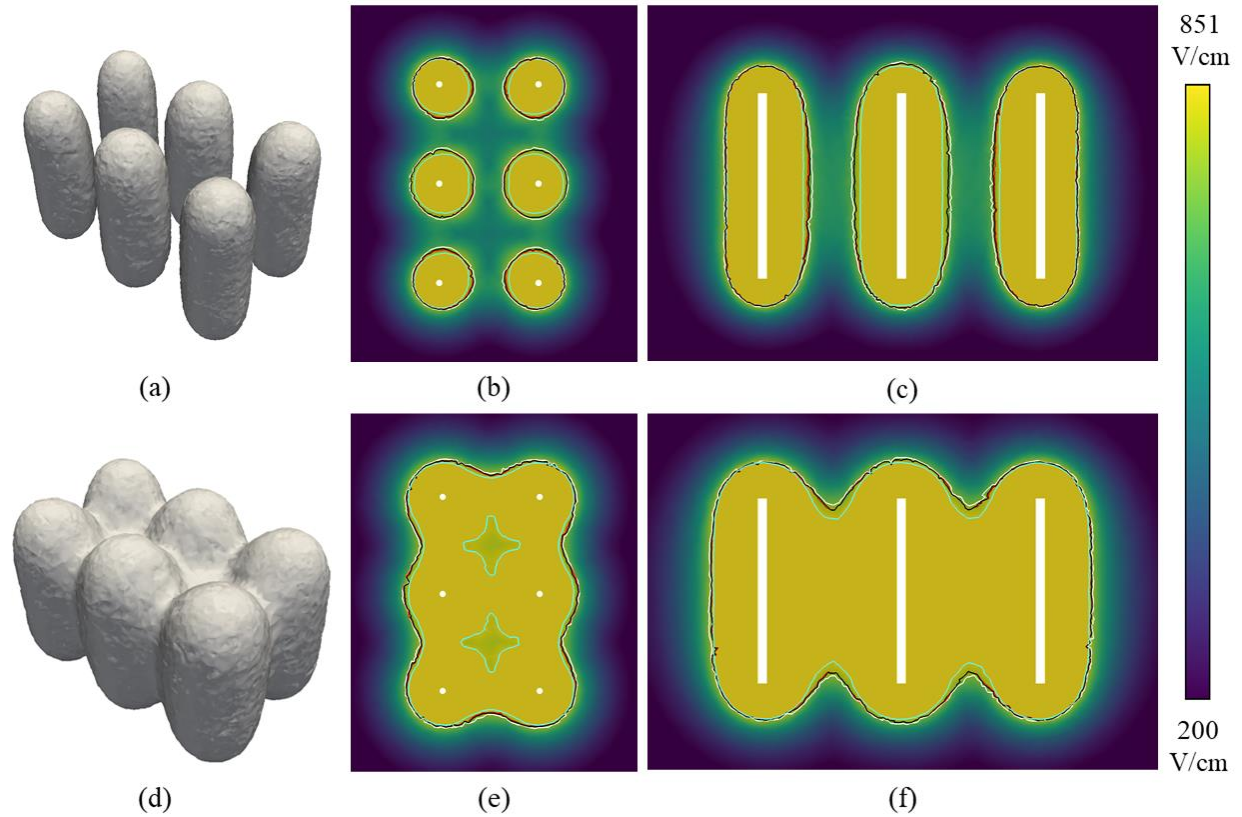
Fig. s.3. Predicted ablated volume in the 6-RECT setup. Electrode spacing is 15 mm and the diameter is 1 mm. (a), (b), and (c) correspond to the treatment at 1000 V/cm voltage to distance ratio, and (d), (e), and (f) correspond to 1500 V/cm one. (a) and (d) display the predicted volume for method C at 10 s inter-treatment pause. (b) and (e) are the transversal cross section and (c) and (f) are the longitudinal cross section with the simulated electric field distribution. The contours correspond to the predicted TV for method A (cyan), method B (red), method C for 1 min inter-treatment pause (black), and method C for 10 s pause (white).
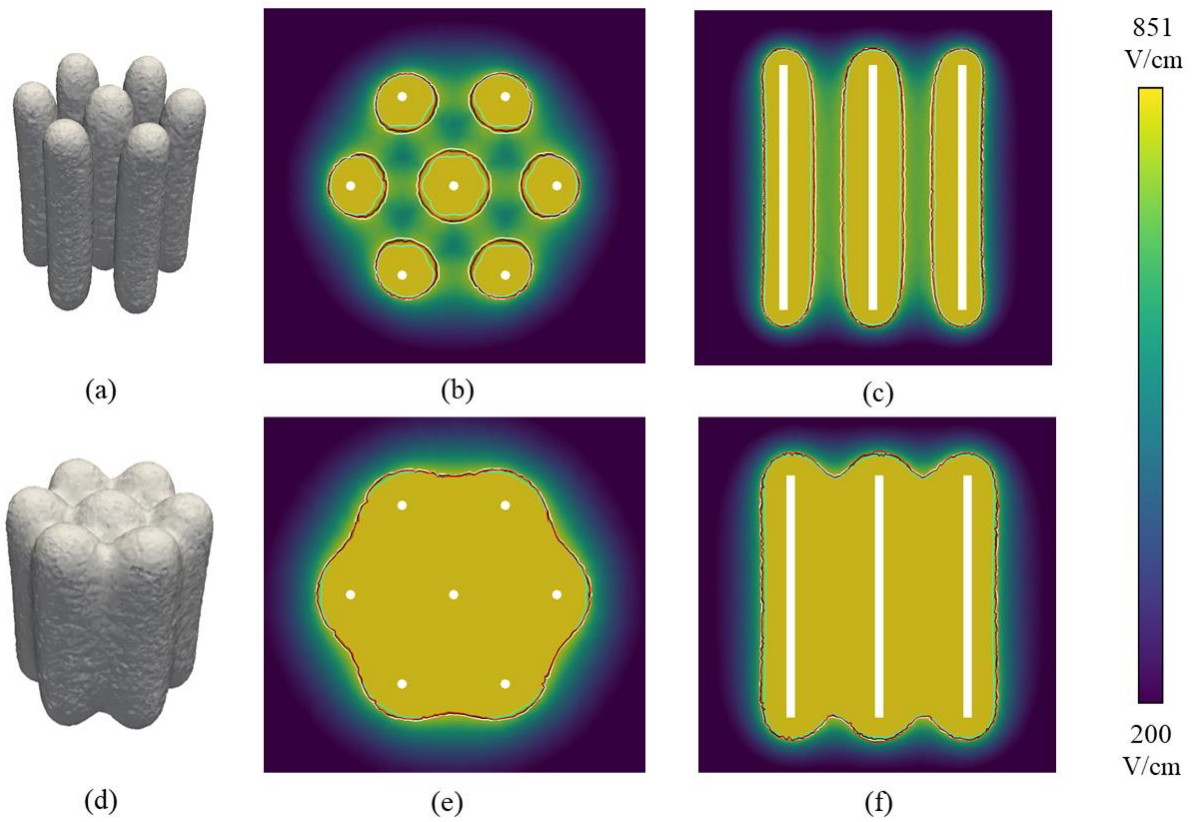
Fig. s.4. Predicted ablated volume in the 7-HEX setup. Electrode spacing is 7.3 mm and the diameter is 0.7 mm. (a), (b), and (c) correspond to the treatment at 1000 V/cm voltage to distance ratio, and (d), (e), and (f) correspond to 1500 V/cm one. (a) and (d) display the predicted volume for method C at 10 s inter-treatment pause. (b) and (e) are the transversal cross section and (c) and (f) are the longitudinal cross section with the simulated electric field distribution. The contours correspond to the predicted TV for method A (cyan), method B (red), method C for 1 min inter-treatment pause (black), and method C for 10 s pause (white).
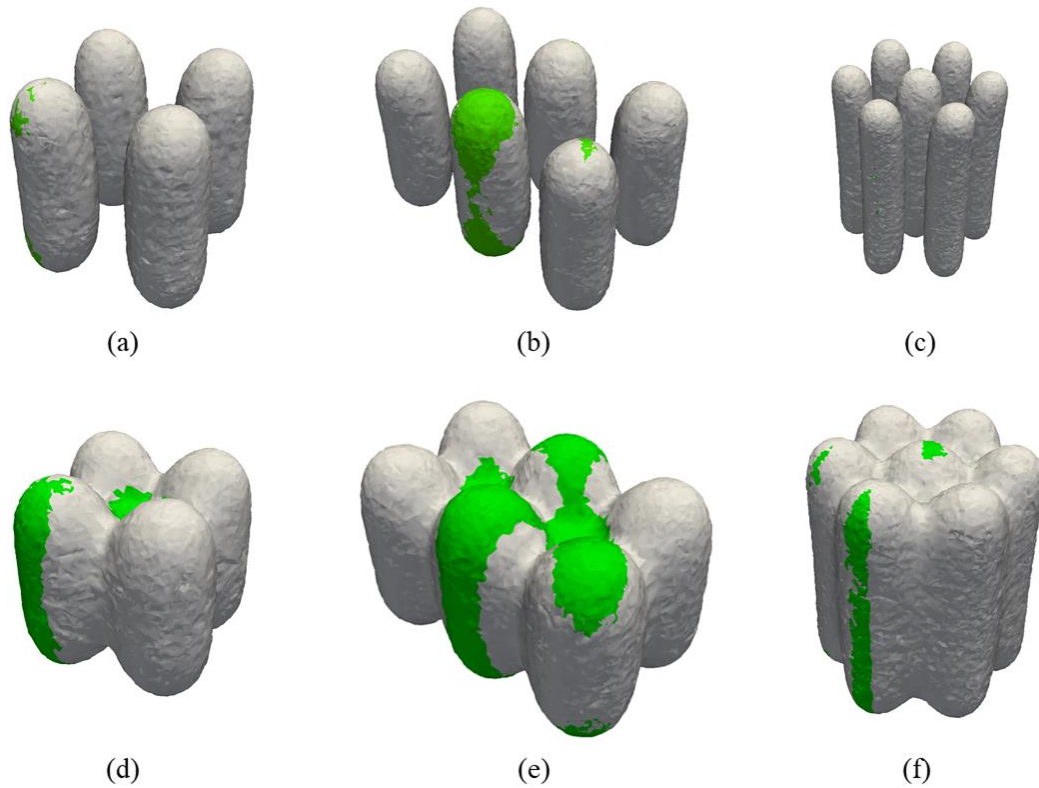
Fig. s.5. Predicted IRE volume (method C at 10 s pause) using two different electrical conductivity. The green isosurface corresponds to the simulation with only in-pulse conductivity changes (s.1) and the white isosurface represents the simulation that also considers the preceding pair conductivity change (s.2). The two surfaces are overlayed on top of each other, and it can be observed that the differences are minimal. The top row (a, b and c) are the simulations at 1000 V/cm voltage to distance ratio, and the bottom row (d, e and f) are at 1500 V/cm. The electrodes configurations are 4-SQ (a, d), 6-RECT (b, e), and 7-HEX (c, f).

**Supplementary material references**

[1]     A. Golberg and B. Rubinsky, "A statistical model for multidimensional irreversible electroporation cell death in tissue," *Biomed. Eng. Online*, vol. 9, Feb. 2010.

[2]     D. Šel *et al.*, "Sequential finite element model of tissue electropermeabilization," *IEEE Trans. Biomed. Eng.*, vol. 52, no. 5, pp. 816–827, May 2005.

[3]     N. Beitel-White *et al.*, "Electrical Characterization of Human Biological Tissue for Irreversible Electroporation Treatments," in *Proceedings of the Annual International Conference of the IEEE Engineering in Medicine and Biology Society, EMBS*, Oct. 2018, vol. 2018-July, pp. 4170–4173.

[4]     A. Ivorra, "Tissue Electroporation as a Bioelectric Phenomenon: Basic Concepts," Springer, Berlin, Heidelberg, 2010, pp. 23–61.